Fibers and Polymers 2002, Vol.3, No.3, 113-119

Flow Behavior at the Embossing Stage of Nanoimprint Lithography

Jun-Ho Jeong*, Youn-Suk Choi[1], Young-Jae Shin, Jae-Jong Lee, Kyoung-Taik Park, Eung-Sug Lee, and Sang-Rok Lee

Department of Intelligent Precision Machine, Korea Institute of Machinery and Materials, Taejon 306-600, Korea
[1]KyungWon Tech Corporation, Seoul 137-841, Korea
(Received July 23, 2002; Revised August 22, 2002; Accepted August 28, 2002)

Abstract: Nanoimprint lithography (NIL) is a nanofabrication method known to be a low cost method of fabricating nano-scale patterns as small as 6 nm. This study is focused on understanding physical phenomena in the embossing of nano/micro scale structures with 100 nm minimum feature size. We present the effects of capillary force and width of stamp groove on flow behavior at the embossing stage through numerical experimentation. We also compare our numerical results with previous experimental results and discuss our results.

Keywords: Nanoimprint lithography, Embossing stage, Capillary force, Surface tension, Numerical simulation

Introduction

The several kinds of nanofabrication methods have been developed for the production of nanostructures. The nanoimprint lithography (NIL), in particular, is known as a low cost method of fabricating nano-scale patterns as small as 6 nm [1]. Compared to NIL, optical lithography is limited due to the light diffraction, scanning probe microscope (SPM) lithography is very slow due to serial processing, and X-ray lithography and focused ion beam (FIB) are expensive.

The NIL process consists of two stages: the embossing stage and the anisotropic etching stage. In the embossing stage, a stamp with nano/micro scale structures is pressed into a thin polymer layer on a substrate, and then is separated from the layer. To minimize air entrapment, the embossing process should be done in a vacuum. During the anisotropic etching stage, the residual polymer is removed completely in the compressed area.

In order for NIL to be in practical applications that require large area patterning and multi-layer patterning beyond laboratory experiments, we need to understand the physical phenomena of the NIL process in detail and to find the optimal conditions for the NIL process parameters, such as pressure, temperature, and processing time. The process conditions at the embossing stage, in particular, directly influence flow behavior, which determines the accuracy of the final geometry of imprinted nano/micro scale structures. In order to investigate flow behavior, previous researches[2-4] based on experimental approaches and simplified theoretical models are reported.

In this study, through numerical experimentation, we present the effects of capillary force and width of stamp groove on flow behavior at the embossing stage. We also compare our numerical results with previous experimental results and discuss physical phenomena at the embossing stage. A commercial computational fluid dynamics (CFD) code based on the finite volume method (FVM), CFD-ACE, is used for simulating filling behavior. In the code, an unsteady incompressible flow with free surfaces is solved on the Eulerian grid by using the full Navier-Stokes momentum equation and the volume of fluid (VOF) method. In order to consider surface tension effects, the high-order nonlinear boundary conditions on a fluid surface are also imposed on free surfaces.

*Corresponding author: jhjeong@kimm.re.kr

Computational Methods

It is known that deviation from the continuum hypothesis for gas media is identified with the Knudsen number

$$N_{\text{Knudsen}} = \frac{\lambda}{L} \tag{1}$$

where λ is the mean-free-path of the molecules and L is a characteristic length scale[5]. The well known Navier-Stokes momentum equation is available for the solution of the velocity and pressure fields, as $N_{\text{Knudsen}} \leq 0.1$. Although similar deviation of the continuum hypothesis occurs for liquids as well, the above concept of mean-free-path does not apply in liquids because the liquid molecules are closely packed. The conditions under which a liquid flow fails to be in the continuum hypothesis are not well defined[5].

Chan and Horn[6] proposed that the Reynolds description of the drainage process for organic liquids appears to be very accurate down to film thickness of about 50 nm. They also showed that the continuum hypothesis breaks down, as the film thickness is less than about ten molecules thick. The dimensions of a polymer molecule-chain are usually characterized by the radius of gyration, R_g, defined as the square root of the average squared distance of all the repeating units of the chain from the center of the mass of the chain. Jackson *et al.*[7] presented the relation between R_g and molecular weight of the polymethylmethacrylate

(PMMA) in tetrahydrofuran (THF) at room temperature as follows:

$$R_g = 0.012\, M^{0.583} \tag{2}$$

where M is the molecular weight. From the above relation, we obtain the value $R_g = 8.34$ nm for the PMMA with $M = 75000$ g/mol as used in Heydermann *et al.*'s experiment [2]. Based on Chan and Horn's results and the value of the R_g computed, we assume that a PMMA of $M = 75000$ g/mol satisfies the continuum hypothesis as $L \geq 100$ nm. This study is focused on understanding physical phenomena in embossing nano/micro scale structures with 100 nm minimum feature size through numerical simulation under the continuum hypothesis.

In this study, a computational method based on the semi-implicit pressure-linked equation algorithm (SIMPLE)[8] is employed for solving the following continuity and Navier-Stokes momentum equations:

The continuity equation:

$$\frac{\partial \rho}{\partial t} + \rho \frac{\partial u_i}{\partial x_i} = 0 \tag{3}$$

The Navier-Stokes momentum equation:

$$\rho \frac{\partial u_i}{\partial t} + \rho u_j \frac{\partial u_i}{\partial x_j} = \frac{\partial}{\partial x_j} \sigma_{ji}(u) + \rho f_i \tag{4}$$

where

$$\sigma_{ij} = -p\delta_{ij} + 2\mu d_{ij}, \quad d_{ij} = \frac{1}{2}\left(\frac{\partial u_i}{\partial x_j} + \frac{\partial u_j}{\partial x_i}\right), \quad i = 1, 2, \text{ and } 3,$$

and $j = 1, 2,$ and 3.

In the above equations, t is the time, u_i is the velocity component in x_i, ρ is the density, μ is the dynamic viscosity, f_i is the body force component in x_i, and σ_{ij} and d_{ij} denote the stress and the strain tensors, respectively.

VOF Method

The VOF method[9] belongs to the category of Eulerian methods. The VOF method has high efficiency for multi-phase flows. In the VOF method, a fractional volume is used to divide the total domain into the fluid and empty (or gas) regions. The values of the fractional volumes in filled cells, partially filled cells, and empty cells are given by unity, between zero and unity, and zero, respectively. The fractional volume is computed at each time step using the advection equation:

$$\dot{f} + u_i \frac{\partial f}{\partial x_i} = 0 \tag{5}$$

where f is the fractional volume and u_i is the velocity component in x_i.

The surface reconstruction procedure is required for computing the fluid volume flux from one element to the neighbor element and for determining surface curvatures. In this study, the piecewise linear interface construction (PLIC) scheme[10] is employed for the surface reconstruction. In the PLIC scheme, the elemental free surface is assumed to be planar and allowed to take any orientation within the element. The unit normal of the elemental free surface plane is determined by assuming that it is parallel to the gradient vector of f. The fluid flux is computed explicitly based on the surface orientation computed at previous time step.

At the initial time step, an initial fractional volume field is specified and the fluid volume fluxes between elements are computed. Then, the volume fractions of fluid elements throughout the total domain at the next time step are calculated using the initial fractional volume of fluid and net transfer of fluid obtained at each element. This procedure for each time step is repeated until the desired final time is reached.

Surface Tension Modeling

Surface tension is generally neglected in macro-scale processing, but, in NIL, surface tension should be considered because it has a dominant influence on flow behavior due to the high surface to volume ratio. Surface tension is created because molecules at the surface of a fluid have higher energy than those in the interior. In order to minimize the potential energy in the fluid, the surface area is minimized. Surface tension causes capillary forces. The direction of the capillary force depends on the wetting of the fluid on the walls. Wetting is characterized by the wetting angle between the fluid surface and the walls.

Assuming that the viscous effect is neglected on a free surface and the surface tension coefficient is constant, the normal force on the surface is equal to the summation of all the tangential force due to surface tension as follows:

$$\int \Delta p \, d\vec{s} = \int \vec{\tau} \, |d\vec{x}| \tag{6}$$

where p is the pressure and $\vec{\tau}$ is the tangential force to be equal to

$$\vec{\tau} = \sigma \vec{n} \times \frac{d\vec{x}}{|d\vec{x}|}. \tag{7}$$

In the above equations σ is the surface tension and $\vec{n}$ is the normal vector. The final form

$$\int \Delta p \, d\vec{s} = \int \sigma \vec{n} \times d\vec{x} \tag{8}$$

is derived from equation (6) and equation (7) and the normal vector $\vec{n}$ is given by

$$\vec{n} = \frac{\nabla \cdot f}{|\nabla \cdot f|}. \tag{9}$$

The wall adhesion boundary condition using the wetting

angle is imposed at the intersection between cavity wall and free surface. The boundary condition becomes an expression for the unit free surface normal $\vec{n}_s$ along the wall:

$$\vec{n}_s = \vec{n}_w \cos\theta + \vec{t}_w \sin\theta \tag{10}$$

where θ is the wetting angle between the fluid and the wall, n_w is the unit wall normal directed into the wall, and t_w lies in the wall and is normal to the contact line between the interface and the wall[10].

Numerical Results

In this numerical experiment, we used the PMMA as a resist material in order to compare our results with Heydermann *et al.*'s experimental results. To simplify our numerical studies we assumed that the embossing stage is isothermal and a stamp moves down with a constant velocity. The density used is 1.17×10^3 kg/m^3[11], viscosity is 3.00×10^3 Pa·s[2], surface tension is 29.7 mN/m[12], and wetting angle is 25 °. The geometry of the computational domain including the stamp and boundary conditions are shown in Figure 1. Assuming that the polymer melt is incompressible and $S \gg h_f$ and h_o, the embossing speeds V_e are computed from the above equations[2]

$$V_e = \frac{(h_o - h_f)}{t_f} = \frac{2p}{\mu S^2}\left(\frac{h_f^2 h_o^2}{h_o + h_f}\right) \tag{11}$$

where h_0 is the initial height of the polymer film, h_f is the final height of the polymer film which is given by $h_f = h_o - WD/(S+W)$, μ is the viscosity, W is the width of stamp

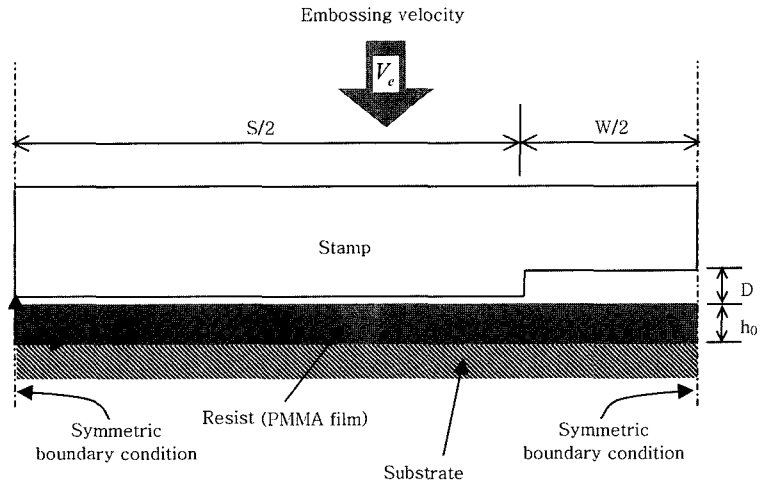

Figure 1. The geometry of computation domain and boundary conditions.

Table 1. Simulation conditions for all cases

Dimension	S (μm)	W (μm)	p (Pa)	D (nm)	h_o (nm)	h_f (nm)	V_e (nm/sec)
2D	60	20	3.6×10^6	175	200	156.25	1.83
2D	30	10	3.6×10^6	175	200	156.25	7.31
2D	30	1	3.6×10^6	175	200	194.35	10.2
2D	30	0.1	3.6×10^6	175	200	199.42	10.6
3D	30	10	6.7×10^5	175	200	189.06	1.83

Table 2. The results obtained for all cases

Dimension	S (μm)	W (μm)	Number of time steps	Number of elements	CPU time (sec)	Processor
2D	60	20	4900	1025	6876	AMD
2D	30	10	2050	515	1463	AMD
2D	30	1	360	535	279	Pentium 4
2D	30	0.1	290	1172	733	Pentium 4
3D	30	10	3400	13405	345600	AMD

groove, D is the depth of stamp groove, S is the width of stamp, and p is the embossing pressure. For all case studies, the embossing speeds computed from equation (11) are given in Table 1. Table 2 shows the number of time steps, number of elements and CPU times consumed for all cases. The time increment Δt is automatically computed from the relation based on the Courant number:

$$N_c = \frac{|V|\Delta t}{d} \leq 0.1 \tag{12}$$

where V is the local velocity and d is the element size. The Δt ranges from 0.0001 sec to 0.01 sec. Because the embossing process is done in a vacuum, the effect of air pressure can be neglected. In order to make the air flow out, we created an artificial outlet with the width $D_0 \approx D/50$ at the middle of the top of the cavity.

In Figure 2, we compare our numerical results with Heydermann *et al.*'s experimental results for the PMMA with $M = 75000$ g/mol. Figure 2(a) shows numerical results for $S = 60\ \mu$m and $W = 20\ \mu$m that correspond to the atomic force microscope (AFM) height profiles[2], respectively. It is shown that the predicted free surface shapes are in excellent agreement with the experimental results. The characteristic length L for this case has a range from 156.25

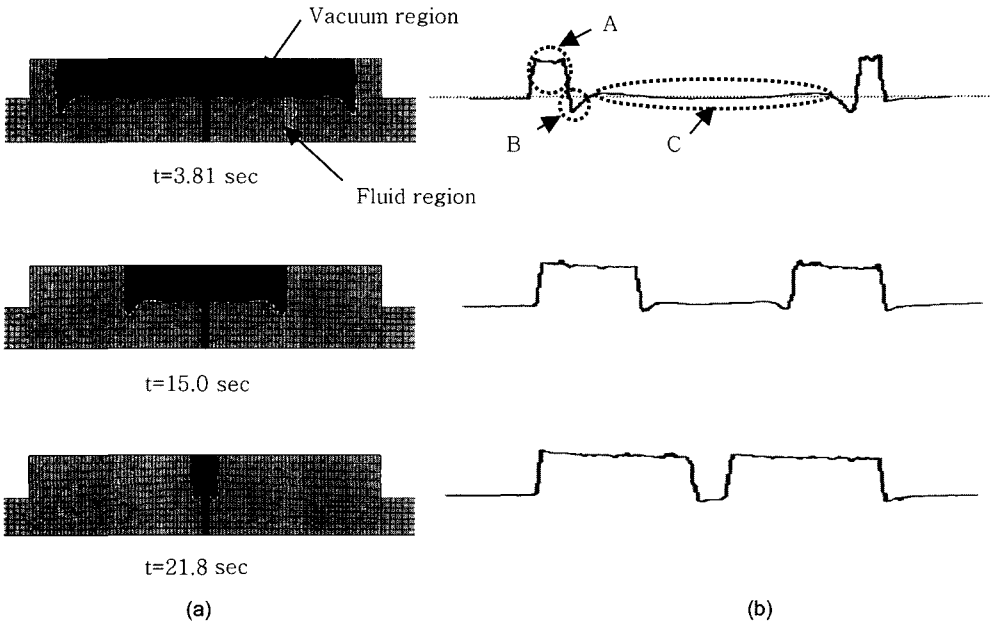

Figure 2. Comparison of simulation results(a) and AFM height profiles(b)[2].

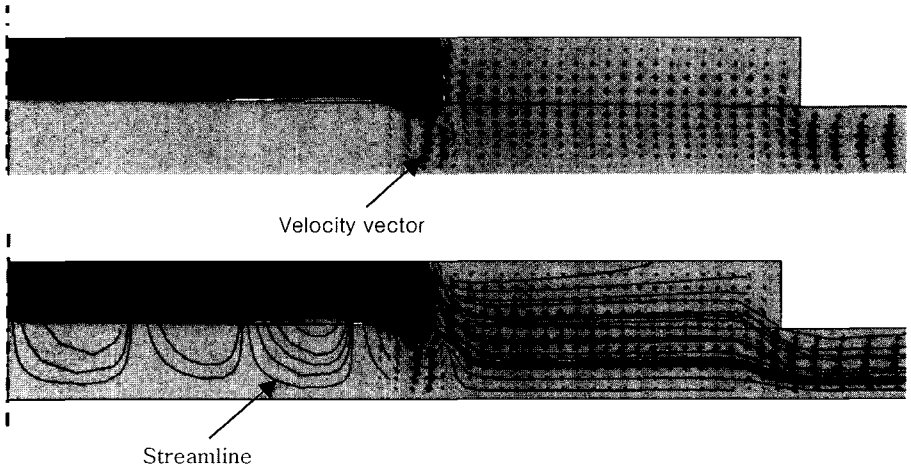

Figure 3. Velocity vector plot and streamline plot at $t = 11.8$ sec.

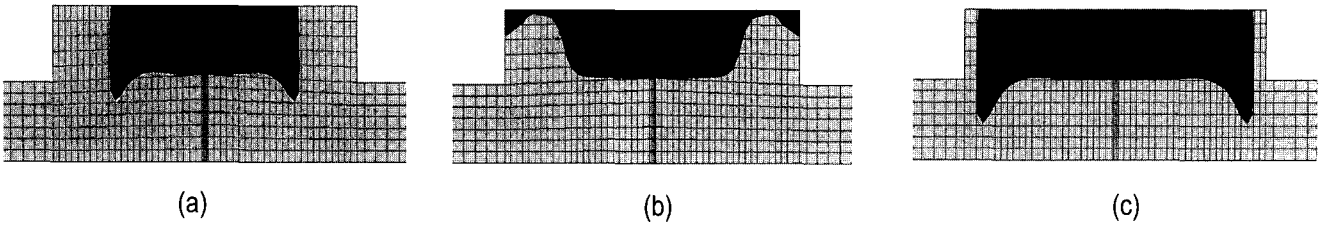

Figure 4. Predicted free surface shapes for $W = 10\ \mu m$. (a) for $\sigma = 29.7$ mN/m and $V_e = 7.31$ nm/s at $t = 2.41$ sec, (b) for $\sigma = 0$ and $V_e = 7.31$ nm/s at $t = 2.46$ sec, (c) for $\sigma = 29.7$ mN/m and $V_e = 0$ at $t = 2.44$ sec.

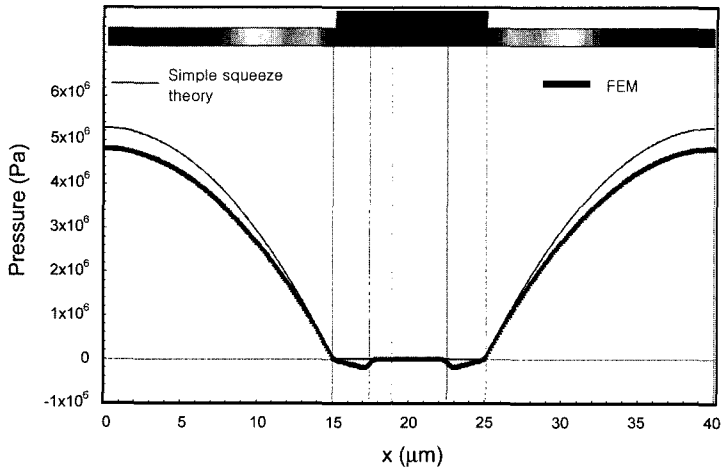

Figure 5. Predicted pressure profiles on the line $y = 90$ nm at $t = 3.06$ sec.

nm to 200 nm because h_0 is equal to 200 nm and the maximum pressing distance of the stamp is 43.75 nm. It is shown from the result that the simulation of the embossing stage under the continuum hypothesis is reasonable at the 100 nm length scale.

As shown in Figure 2(b) the cavity region can be divided into three kinds of regions: the upstream region, A; the concave region, B; and the center region, C. In region A, the capillary force and squeezing pressure affect the free surface shape. The capillary force also dominantly affects the flow in region B. In region C, which has an almost flat surface, small-scale flow fields exist with local compression mode field. Figure 3 shows the plots of velocity vectors and streamlines at $t = 11.8$ sec for $S = 60\ \mu m$ and $W = 20\ \mu m$. We can see that the maximum velocities appear in region B and in the interface between the region A and air. It is also shown that the back flow is created in region B.

Figure 4 shows the obvious effect of the capillary force on filling behavior. Figure 4(a) is the free surface shape for the simulation with $V_e = 1.83$ nm/sec and $\sigma = 29.7$ mN/m, and Figure 4(b) is the result for the simulation with $V = 1.83$ nm/sec and no surface tension. The PMMA melt is completely filled at the corner of the cavity in Figure 4(a), but it is not filled at the corner in Figure 4(b). The interface between region B and air is almost vertical in Figure 4(a), while the interface is inclined at about 30° to the vertical in Figure 4(b). We can also see the concave region only in Figure 4(a). In addition, we simulated the case of $V_e = 0$ and $\sigma = 29.7$ mN/m. Figure 4(c) shows that the concave region is formed by the capillary force. For the simulation with no embossing speed, the interface does not move from 1.40 sec and keeps its position because there is no inflow from outside.

In Figure 5, it is shown that the predicted pressure profile on the line $y = 90$ nm at $t = 3.06$ for $S = 30\ \mu m$ and $W = 10\ \mu m$ agrees with the following theoretical solution for a simple squeeze flow:

$$p = \frac{3\dot{h}\mu s^2}{h^3}\left(\frac{x^2}{s^2} - 1\right) \tag{13}$$

Figure 5 also shows that negative pressure field occurs in the expansion flow region, Part II.

In order to understand three-dimensional (3D) flow behavior at the embossing stage, a 3D simulation for $S = 30\ \mu m$ and $W = 10\ \mu m$ was carried out. Considering the geometry of the 3D cavity, the h_f for the 3D simulation is computed as follows:

$$h_f = h_o - \frac{DW^2}{(S + W)^2}. \tag{14}$$

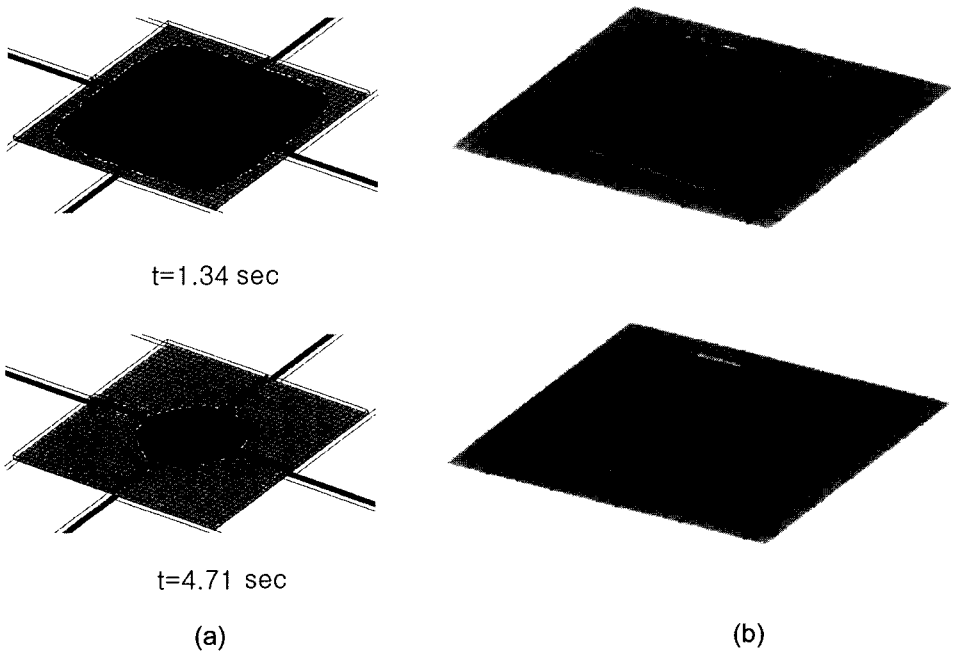

Figure 6. Comparison of 3D simulation results(a) and 3D AFM height profiles(b)[2].

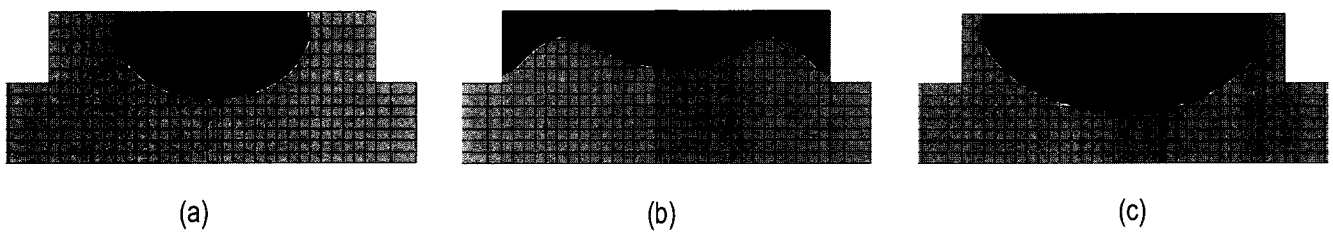

Figure 7. Predicted free surface shapes for $W = 1$ μm. (a) for $\sigma = 29.7$ mN/m and $V_e = 10.2$ nm/s at $t = 0.220$ sec, (b) for $\sigma = 0$ and $V_e = 10.2$ nm/s at $t = 0.236$ sec, (c) for $\sigma = 29.7$ mN/m and $V_e = 0$ at $t = 0.276$ sec.

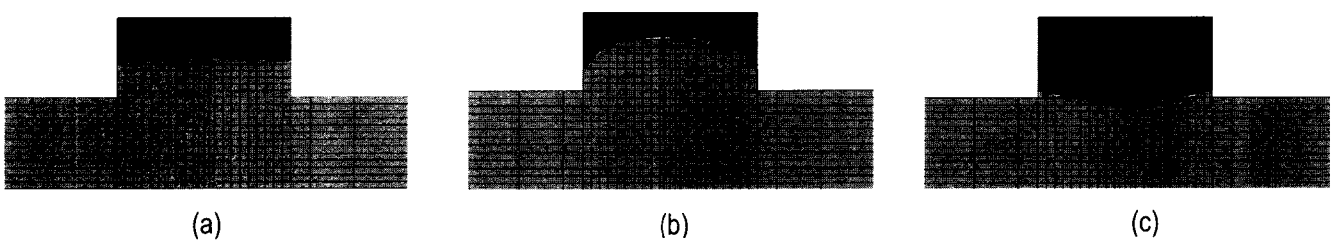

Figure 8. Predicted free surface shapes for $W = 100$ nm. (a) for $\sigma = 29.7$ mN/m and $V_e = 10.6$ nm/s at $t = 0.0275$ sec, (b) for $\sigma = 0$ and $V_e = 10.6$ nm/s at $t = 0.0259$ sec, (c) for $\sigma = 29.7$ mN/m and $V_e = 0$ at $t = 0.0288$ sec.

The V_e is given as 1.83 nm/sec as with the case of the above two-dimensional (2D) simulation for $S = 60$ μm and $W = 20$ μm. The simulation results are compared with the 3D AFM images[2] for $S = 60$ μm and $W = 20$ μm in Figure 6. The predicted free surface shapes are in good agreement with the experimental results, even though the domain size of the simulation is different from that of the experiment. From the comparison between the 2D results in Figures 2(a) and 4(a), we can predict that the predicted 3D free surface for the $S = 60$ μm and $W = 20$ μm will be very similar to that for $S = 30$ μm and $W = 10$ μm. We did not simulate the case for $S = 60$ μm and $W = 20$ μm because the simulation would have required too much computation time. We consumed about 96 hours for the 3D simulation for $S = 30$ μm and

$W = 10\ \mu m$.

To investigate the effect of width of stamp groove on flow behavior, we also simulated cases of $W = 1\ \mu m$ and $W = 100$ nm. In both cases, the is given as 30 μm as with the case of the $W = 10\ \mu m$. It is shown that the free surface shape is dramatically changed according to the groove width in Figures 4, 7, and 8. Figure 7(a) shows that the free surface shape for the case of $W = 1\ \mu m$ maintains a single curved shape and has no local concave region. This result occurs because the used is too small to make a double-well shape through surface tension alone as shown in Figure 7(c) and the distance between the two peaks of two-humped shape created only by viscous flow is too short as shown in Figure 7(b). In the case of $W = 100$ nm, the free surface has a totally convex interface as shown in Figure 8. The reason for this result is that the W used is too small to make a two-humped shape by viscous flow as shown in Figure 8(b) and the viscous flow is much faster than the capillary flow due to the high embossing speed and small groove width to be used for the simulation.

Conclusions

In order to understand physical phenomena in embossing nano/micro-scale structures with 100 nm minimum feature size, a numerical experiment using a commercial CFD code, CFD-ACE, has been carried out. From Jackson *et al*'s[7] relation between the radius of gyration R_g and molecular weight M, we obtained the value $R_g = 8.34$ nm for the PMMA with $M = 75000$ g/mol as used in Heydermann *et al*.'s experiment[2]. Based on the value of the R_g computed and Chan and Horn's experimental results[6], we assumed that a PMMA of $M = 75000$ g/mol satisfies the continuum hypothesis as $L \geq 100\ nm$ ($>R_g \times 10$). Through the comparison between our numerical result and Heydermann *et al*.'s experimental result, it has been shown that the numerical simulation of the embossing stage under the continuum hypothesis is reasonable at a 100 nm length scale. Through several numerical case studies, we have also presented that the flow behavior in the embossing stage is dominantly affected by the capillary force and width of stamp groove.

References

1. S. Y. Chou, P. R. Krauss, W. Zhang, L. Guo, and L. Zhuang, *J. Vac. Sci. Technol. B*, **15**, 2897 (1997).
2. L. J. Heydermann, H. Schift, C. David, J. Gobrecht, and T. Schweizer, *Microelectronic Engineering*, **54**, 229 (2000).
3. H. C. Sheer and H. Schulz, *Microelectronic Engineering*, **56**, 311 (2001).
4. X. J. Shen, L. W. Pan, and L. Lin, *Sensors and Actuators A*, **97-98**, 428 (2002).
5. A. Beskok, W. Trimmer, and G. E. Karniadakis, *J. Fluid Eng.*, **118**, 448 (1996).
6. D. Y. C. Chan and R. G. Horn, *J. Chem. Phys.*, **83**, 5311 (1985).
7. C. Jackson, Y. J.Chen, and J. W. Mays, *J. Appl. Polym. Sci.*, **61**, 865 (1996).
8. S. Parakar, "Numerical heat transfer and fluid flow", Heisphere Publishing Corp., McGraw Hill, New York, 1980.
9. C. Hirt and B. Nichols, *J. Comp. Phy.*, **39**, 201 (1981).
10. D. B. Koth and R. C. Mjolsness, *AIAA Journal*, **30**, 2694 (1992).
11. Z. Tadmor and C. Gogos, "Principles of polymer processing", Wiley, New York, 1970.
12. E. Schaffer, Ph. D. Thesis, University of Groningen, Groningen, 2001.